Strength and Breaking Mechanism of Multiwalled Carbon Nanotubes Under Tensile Load

Min-Feng Yu,[1] Oleg Lourie,[1] Mark J. Dyer,[2] Katerina Moloni,[3] Thomas F. Kelly,[3] Rodney S. Ruoff[1]*

The tensile strengths of individual multiwalled carbon nanotubes (MWCNTs) were measured with a "nanostressing stage" located within a scanning electron microscope. The tensile-loading experiment was prepared and observed entirely within the microscope and was recorded on video. The MWCNTs broke in the outermost layer ("sword-in-sheath" failure), and the tensile strength of this layer ranged from 11 to 63 gigapascals for the set of 19 MWCNTs that were loaded. Analysis of the stress-strain curves for individual MWCNTs indicated that the Young's modulus *E* of the outermost layer varied from 270 to 950 gigapascals. Transmission electron microscopic examination of the broken nanotube fragments revealed a variety of structures, such as a nanotube ribbon, a wave pattern, and partial radial collapse.

Theoretical analysis predicts that ideal single-walled carbon nanotubes (SWCNTs) should possess extremely high tensile strengths (*1*). The strain at tensile failure has been predicted to be as high as ~30% for SWCNTs (*2*), and thus a tensile strength of ~300 GPa would be expected if the in-plane Young's modulus *E* (~1000 GPa) of graphite were used (*3*), and the axial *E* of some SWCNTs might even exceed this value (*4*–*6*). A recent and more sophisticated model of mechanical relaxation of SWCNTs describes a mechanism of defect nucleation in which two hexagon pairs are converted, through Stone-Wales bond rotation, into 5-7-7-5 (pentagon-heptagon) defects that can then migrate in the nanotube (*1, 7*). Strength is then predicted to be a function of both nanotube structure (chirality and diameter) and of parameters such as temperature and strain rate (*1*, *7*–*10*).

Previous methods for measuring the mechanics of individual carbon nanotubes include observing the thermally induced or electric field–induced vibration of "cantilevered" nanotubes inside a transmission electron microscope (TEM) (*11*, *12*), measuring the lateral bending of suspended multiwalled carbon nanotubes (MWCNTs) (*13*, *14*) or of SWCNT ropes (*15*) with atomic force microscopy (AFM), measuring axial compression with tapping-mode AFM (*16*), and examining the pattern of mechanically deformed MWCNTs in polymer composites with a TEM (*17, 18*). Axial *E* values ranging from ~200 to ~4000 GPa, an average bending strength of ~14 GPa, axial compressive strengths of ~100 GPa for MWCNTs, and strain at failure of ~0.05 for SWCNT ropes were obtained in these studies. Carbon nanotubes are thus potentially the ultimate fiber for high-strength materials applications such as composite reinforcement or cable components.

We have measured the stress-strain response and strength-at-failure of individual arc-grown MWCNTs under tensile loading. Tensile-loading experiments with individual nanotubes has not been done before because of their small size; whiskers and fibers having diameters on the order of micrometers have been loaded in pure tension (*19*). We have developed and built a manipulation tool that can also be used as a mechanical loading device; it operates inside a scanning electron microscope (SEM) (*20*–*22*). Individual MWCNTs were picked up and then attached at each end of a section length onto the opposing tips of AFM cantilever probes. Each nanotube section was then stress-loaded and observed in situ in the SEM (a LEO 982 FE-SEM was used). Each tensile-loading experiment was recorded on video, and the data were later analyzed after conversion of the video frame images to computer files.

After the MWCNTs broke, the AFM cantilevers with attached nanotube fragments were transferred to a TEM sample stage and examined in the TEM (a JEOL FX 2000 TEM was used, at an operating voltage of 200 kV) to determine accurately the inner and outer diameters (IDs and ODs) and to identify, if possible, any structural changes. The AFM probes used in these experiments provide a sharp end for picking up and mounting each nanotube, and they act as force sensors through the imaging of the cantilever deflection. The SEM images of a nanotube linked between two opposing AFM tips before tensile loading are shown in Fig. 1. In the experiment, a soft AFM probe {a cs12 contact mode AFM probe with a nominal force constant less than 0.1 N/m [Molecular Devices and Tools for Nanotechnology (NT-MDT)]} and a rigid AFM probe (either a Digital Instruments TESP probe tip or a NT-MDT cs12 noncontact mode probe) were used. The rigid cantilever (top cantilever, Fig. 1) was driven by the *y* linear picomotor of the tensile-loading stage, and the soft cantilever (lower cantilever, Fig. 1) bent from the tensile load applied to the nanotube linked between the AFM tips. By recording the whole tensile-loading experiment, both the deflection of the soft cantilever [the force applied on the nanotube (*23*)] and the length change of the nanotube were simultaneously obtained (Fig. 2A).

Firm nanotube attachment onto the AFM tips is critical. The small sample size precludes conventional methods of attachment such as strong adhesives or grips or both that are used for measuring the tensile strengths of larger diameter whiskers (*17*). However, solid carbonaceous material can be deposited in electron microscopes onto surface regions where the electron beam repeatedly scans (*24*, *25*). The deposition rate depends on imaging parameters, the vacuum quality, and the surface contamination of the sample. Two processes are reported to be involved in the deposition. One is the dissociation of the residual organic species inside the SEM chamber by the electron beam, followed by the subsequent deposition onto the surface; another is the migration of the organic contamination on the sample surface toward the focused point of the electron beam, followed by dissociation and deposition (*24*, *25*). We exploited this method of making a solid carbonaceous deposit to locally attach nanotubes onto the AFM tips. A deposit at least 100 nm square was typically made at each MWCNT/AFM tip interface and was usually a strong enough attachment to allow the loading and breaking of MWCNTs before the attachment failed (*20*–*22*). For the MWCNTs in the current sample set, about half would become detached at one of the deposit sites during the tensile-loading experiment. We report here the results from the successful mounting, tensile loading, and breaking of 19 MWCNTs.

The majority of the MWCNT fragments after breakage projected essentially straight out from each AFM tip, but sometimes curled MWCNT fragments were found that evidently were the remains of MWCNT fracture. Two series of SEM images of two individual

[1]Department of Physics, Washington University in St. Louis, CB 1105, St. Louis, MO 63130, USA. [2]Zyvex LLC, Suite 200, 1321 North Plano Road, Richardson, TX 75081, USA. [3]Department of Materials Science and Engineering, University of Wisconsin, 1509 University Avenue, Madison, WI 53706, USA.

*To whom correspondence should be addressed. E-mail: ruoff@wuphys.wustl.edu

MWCNTs captured before and after breaking are shown in Fig. 3. In the first series (Fig. 3, A through C), a ~6.9-μm-long section of a MWCNT (Fig. 3A) was stretched and broken in the middle. The resulting fragment attached on the top AFM tip (Fig. 3B) had a length of at least 6.6 μm, whereas the fragment on the lower AFM tip (Fig. 3C) had a length of at least 5.9 μm. The quoted fragment lengths are lower limits because of parallax effects in imaging. Thus, the sum of the fragment lengths far exceeded the original section length. This apparent discrepancy can be explained by a "sword-in-sheath"–type fracture mechanism, similar to that observed in carbon fibers (*26*).

In another example of sword-in-sheath failure, a tensile-loaded MWCNT with a section length of ~11 μm (Fig. 3D) suddenly converted to an S-shaped ~23-μm-long section (Fig. 3E). The apparent extraordinary increase in length was because the outermost layer fractured before the inner section had been totally pulled out. When the outer layer broke, the lower cantilever rebounded to its initial position from a deflection of ~10 μm just before breaking. We attempted to measure the force needed to pull out the inner shell from the outer shell by moving the rigid cantilever upward. No deflection of the lower soft cantilever could be observed, which for this imaging magnification corresponded to a force less than 10 nN (*27*). After being completely pulled out, the upper fragment was at least 22 μm long, whereas the lower fragment was ~10 μm long, which shows that the pulled-out section extended well beyond the attachment site before breaking. Evidently, for this particular MWCNT, there was a long section extending below the attachment site on the lower tip. The bulk sample consisted of MWCNTs with a typical length around 30 μm, which is significantly longer than the gauge lengths of MWCNTs that were tensile-loaded (Table 1). Of the 19 fractured MWCNTs, 16 clearly had a fragment length sum far exceeding the section length just before breaking. We could not evaluate any extra "pullout" length for the other three MWCNTs (which broke very near the attachment point). The sword-in-sheath breaking mechanism is therefore a common failure mechanism for MWCNTs loaded in this way.

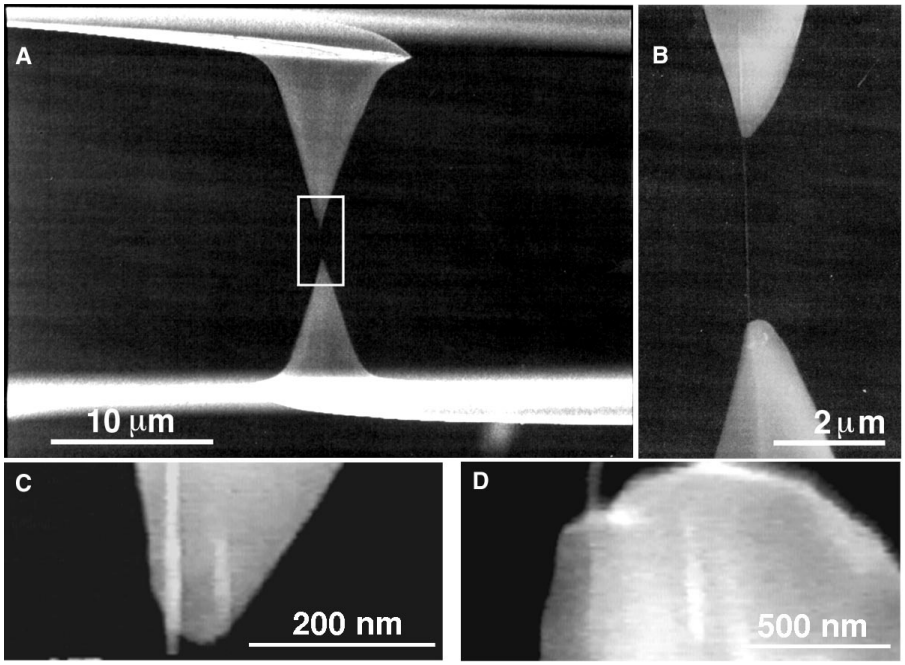

Fig. 1. An individual MWCNT mounted between two opposing AFM tips. (**A**) An SEM image of two AFM tips holding a MWCNT, which is attached at both ends on the AFM silicon tip surface by electron beam deposition of carbonaceous material. The lower AFM tip in the image is on a soft cantilever, the deflection of which is imaged to determine the applied force on the MWCNT. The top AFM tip is on a rigid cantilever that is driven upward to apply tensile load to the MWCNT. (**B**) High-magnification SEM image of the indicated region in (A), showing the MWCNT between the AFM tips. (**C**) Higher magnification SEM image showing the attachment of the MWCNT on the top AFM tip. There is an apparent thickening of the MWCNT section on the surface. (**D**) Close-up SEM image showing the attachment of the MWCNT on the lower AFM tip. The MWCNT section is covered by a square-shaped carbonaceous deposit.

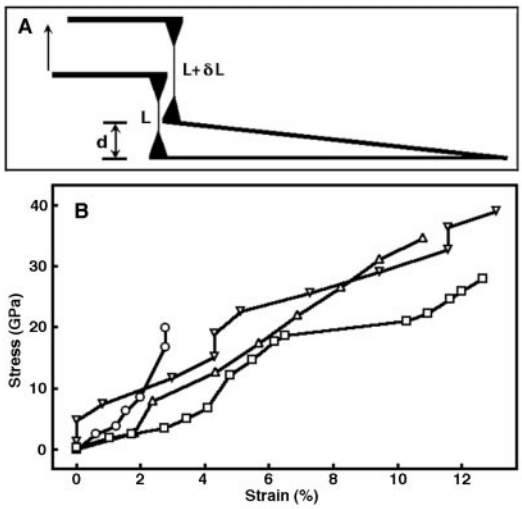

Fig. 2 (**A**) Schematic showing the principle of the tensile-loading experiment. When the top cantilever is driven upward, the lower cantilever is bent upward by a distance d, while the nanotube is stretched from its initial length of L to $L + \delta L$ because of the force exerted on it by the AFM tips. The force is calculated as kd, where k is the force constant of the lower cantilever. The strain of the nanotube is $\delta L/L$. (**B**) Plot of stress versus strain curves for individual MWCNTs. The E values in Table 1 are as follows: 954 GPa from a linear fit to the upswing part of the curve for nanotube 2 (○); linear fits of the first (470 GPa) and the second (300 GPa) upswings for nanotube 15 (□), and 335 and 274 GPa from linear fits of the whole curve for nanotubes 18 (Δ) and 19 (∇).

Table 1 shows the gauge length (the section length before loading, L_0) of each MWCNT, the ID and OD of each MWCNT as determined by TEM, the applied force (F) at which each MWCNT broke, and the tensile strength (σ_s) calculated from the cross-sectional area S of the outermost layer of the MWCNT [$S = \pi(\mathrm{OD})d$, where d is the interlayer separation of graphite, 0.34 nm]. The measured tensile strengths of the outermost layer of each MWCNT ranged from ~11 to

~63 GPa. There was no apparent dependence of tensile strength on the outer shell diameter. These values, although lower than theoretical predictions for a perfect SWCNT, are still significantly higher than the tensile strengths of conventional carbon fibers (*30*). Tensile strengths up to 20 GPa were reported for graphite whiskers (*28*), which were stated to have a scroll-like structure rather than the "Russian doll" structure (nested cylinders) often observed in MWCNTs.

There is an inverse relation between stiffness (Young's modulus E) and tensile strength for the four MWCNTs for which we have obtained values of E for the outer cylinder. This is often also observed for conventional carbon fibers of significantly larger diameter than the MWCNTs studied here. Further work on measuring E and σ_s for a much larger set of MWCNTs is needed to see whether this is indeed a general property of arc-grown carbon MWCNTs.

There could be several contributing factors to the measured tensile strengths being lower than theoretical predictions for perfect SWCNTs. If structural defects exist in the outer shell of the MWCNTs loaded here, which were produced by the arc discharge method, their strengths could be significantly lower as compared to the defect-free case. During elongation of a SWCNT, there will naturally be some diameter reduction. In a MWCNT, that reduction may be halted (or retarded) by the reinforcing of the inner shells. The presence of small twist or shear loads or both in our current method is also possible; removing these limitations entirely is an area for future improvement. Our ability to see small twist or bending moment effects is currently limited by several factors, including the flexibility of these MWCNTs, which means that they might undergo slight twisting upon attachment, for example, and the possibility that the MWCNT is not perfectly aligned initially with the tensile-loading direction. Finally, neither theory or experiment has yet fully assessed the influence of either strain rate or defects on strength.

The Young's modulus values of the outer layer obtained from the stress-strain curves of MWCNTs (Fig. 2B) range from ~270 to ~950 GPa. The measured strain at failure can be as high as ~0.12 (12% change in length) (Fig. 2). Nominal (or "engineering") tensile strengths and the E values based on the cross-sectional area of the full specimen are significantly lower and range from ~1.4 to ~2.9 GPa for the nominal tensile strengths and from ~18 to ~68 GPa for the Young's modulus values.

Our TEM examination of the broken MWCNT fragments revealed a variety of structural patterns (Fig. 4). They are presented as examples of what happens as a result of either the tensile loading or the fracture event. Vibration of the long thin MWCNT sections sticking out from the AFM tip hindered high-resolution imaging. We observed several MWCNT fragments that showed a wavelike structure on both sides in the TEM image (Fig. 4, A and B); this

Table 1. Partial list of the MWCNTs tested in the tensile-loading experiment [the full list is given online (*21*)]. Shown are the nanotube number, gauge length, IDs and ODs, force applied at fracture, and the tensile strength calculated for the outermost cylinder. The ID of some of the MWCNTs could not be determined (indicated by dashes). Number 15 was one of only three nanotubes for which the sum of the fragment lengths did not greatly exceed the section length just before breaking.

MWCNT number	L_0 (μm)	ID (nm)	OD (nm)	F (nN)	σ_s (GPa)
2	6.50	–	19	400	20
5	6.87	–	20	1340	63
6	10.99	9.5	33	810	21
10	1.80	10	36	920	24
15	2.92	–	13	390	28
18	6.67	4	22	810	35
19	6.04	4	22	920	39

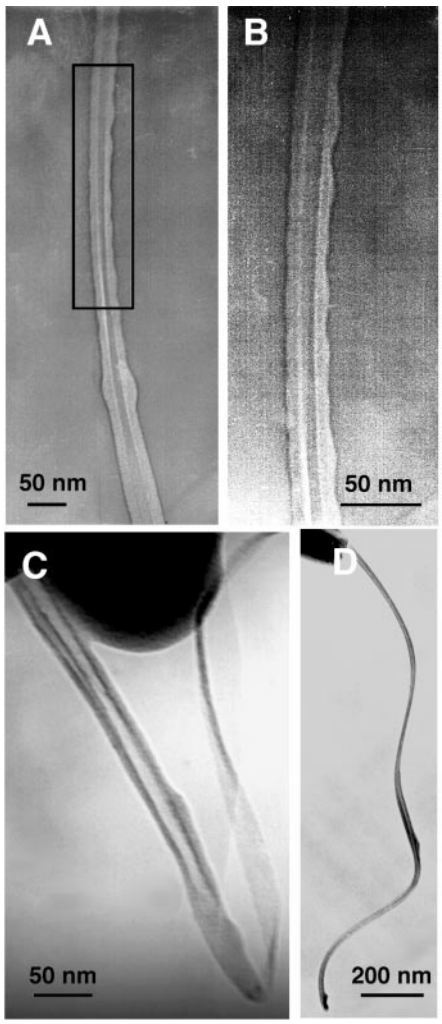

Fig. 4. TEM images of fracture structures of several MWCNT fragments. (**A**) TEM image of a MWCNT (number 6) fragment having a wave pattern along the outer surface. (**B**) TEM image of the wave pattern of the same fragment at high magnification, corresponding to the indicated region in (A). (**C**) A thin-walled, twisted and collapsed MWCNT fragment from the fracture of MWCNT number 2. (**D**) A collapsed MWCNT (number 5) fragment on an AFM tip.

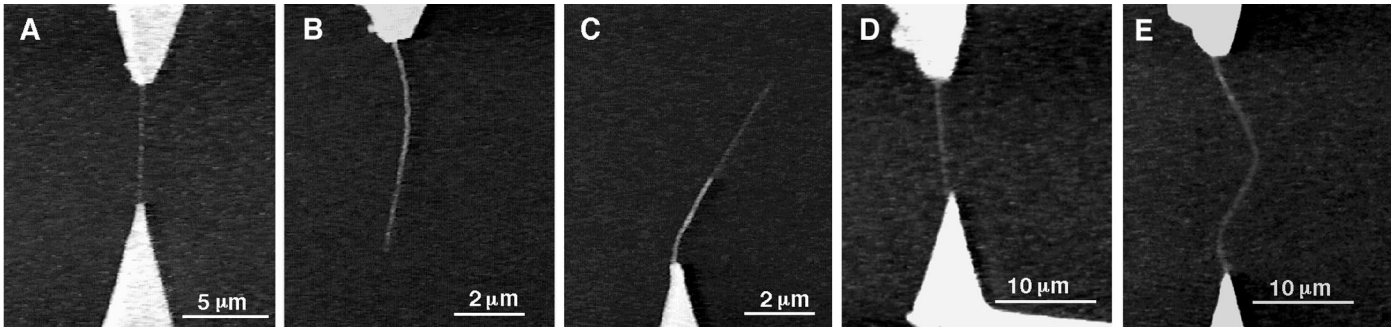

Fig. 3. Fracture of two individually loaded MWCNTs captured in two series of SEM images. The first series shows (**A**) a MWCNT having a section length of ~6.9 μm under tensile load just before breaking. (**B**) After breaking, one fragment of the same MWCNT was attached on the upper AFM tip and had a length of ~6.6 μm. (**C**) The other fragment of the same MWCNT was attached on the lower AFM tip and had a length of ~5.9 μm. In the second series, (**D**) shows another MWCNT having a section length of ~11 μm under tensile load before breaking. (**E**) The same MWCNT with an S shape immediately after fracture; it now has a length of ~23 μm, and the lower cantilever has deflected back to its initial (relaxed) position, indicating the partial pullout of the two nanotube fragments after breaking. In these two examples of fracture events, the fact that the sum of the fragment lengths far exceeds the section length just before break is explained by the sword-in-sheath fracture mechanism.

permanent wavelike deformation only occured on the outer surface of these MWCNTs. We speculate that when the outer layer of the MWCNT breaks at these large stresses, the accumulated elastic energy is released and generates a stress wave; the stress wave travels through the outer surface of the MWCNT and permanently deforms it (*31*). A second possibility is that an accordia-like relaxation of the outer shell onto the inner section occurred immediately after the breaking of the outer shell. Ribbon-like structures were also often seen in the TEM images of the MWCNT fragments (Fig. 4C) and might result in the section of the outer shell from which the inner section has been pulled out. Radial collapse of the MWCNT fragment (Fig. 4D) was also seen. At high tensile strain, the MWCNT experiences a Poisson contraction, which could trigger radial collapse. Partial, and total, radial collapse of MWCNTs has been previously reported (*16*, *32*, *33*). Observation of these types of fragments suggests that the effect of large tensile load and of fracture on nanotube structure will be a fascinating area for further study. Future directions include attempting mechanical-loading measurements on SWCNT ropes and individual SWCNTs, as well as on other types of nanotubes such as boron nitride, and studying the influence of strain rate, temperature, and chemical environment.

References and Notes

1. B. I. Yakobson, in *Fullerenes—Recent Advances in the Chemistry and Physics of Fullerenes and Related Materials*, R. S. Ruoff and K. M. Kadish, Eds. (Electrochemical Society, Pennington, NJ, 1997), vol. 5 (97–42), pp. 549–560.
2. _____, M. P. Campbell, C. J. Brabec, J. Bernholc, *Comput. Mater. Sci.* **8**, 341 (1997). The strain rate in this computer simulation was extremely high.
3. B. T. Kelly, *Physics of Graphite* (Applied Science, London, 1981).
4. B. I. Yakobson, C. J. Brabec, J. Bernholc, *Phys. Rev. Lett.* **76**, 2511 (1996).
5. J. P. Lu, *J. Phys. Chem. Solids* **58**, 1679 (1997).
6. R. S. Ruoff and D. C. Lorents, *Carbon* **33**, 925 (1995).
7. B. I. Yakobson, *Appl. Phys. Lett.* **72**, 918 (1998).
8. P. Zhang, P. E. Lammert, V. H. Crespi, *Phys. Rev. Lett.* **81**, 5346 (1998).
9. M. Buongiorno Nardelli, B. I. Yakobson, J. Berhholc, *Phys. Rev. B* **57**, R4277 (1998).
10. _____, *Phys. Rev. Lett.* **81**, 4656 (1998).
11. P. Poncharal, Z. L. Wang, D. Ugarte, W. A. de Heer, *Science* **283**, 1513 (1999).
12. A. Krishnan, E. Dujardin, T. W. Ebbesen, P. N. Yianilos, M. M. J. Treacy, *Phys. Rev. B Condens. Matter Mater. Phys.* **58**, 14031 (1998).
13. E. W. Wong, P. E. Sheehan, C. M. Lieber, *Science* **277**, 1971 (1997).
14. J.-P. Salvetat *et al.*, *Adv. Mater. (Weinheim, Ger.)* **11**, 161 (1999).
15. D. A. Walters *et al.*, *Appl. Phys. Lett.* **74**, 3803 (1999).
16. M. F. Yu, T. Kowalewski, M. J. Dyer, R. S. Ruoff, in preparation.
17. O. Lourie, D. M. Cox, H. D. Wagner, *Phys. Rev. Lett.* **81**, 1638 (1998).
18. H. D. Wagner, O. Lourie, Y. Feldman, R. Tenne, *Appl. Phys. Lett.* **72**, 188 (1998).
19. A. P. Levitt, *Whisker Technology* (Wiley-Interscience, New York, 1970).
20. M. F. Yu *et al.*, *Nanotechnology* **10**, 244 (1999).
21. Experimental details are available at *Science* Online at www.sciencemag.org/feature/data/1046083.shl.
22. The SEM nanostressing stage mainly consists of two parts. One is an *x-y* sliding stage driven by two linear picomotors, with a quadrant piezotube on top; another is a *z* stage driven by a linear picomotor, with a theta stage driven by a rotating picomotor on top. The linear picomotor has a step size of about 30 nm, and the rotating picomotor has a step resolution of better than 0.1 mrad. The stage can travel 6 mm in three dimensions and rotates continuously in the θ direction along the *x* axis. All picomotors were driven with a control pad that can manually set constant velocities for the extension and retraction of the picomotor driving shaft. The piezotube can give subnanometer resolution in three axes with several microns of travel range. Operation of the stage inside the SEM showed smooth travel and no interference with the SEM imaging. The LEO 982 FE-SEM has a stated resolution of 1 nm at an operating voltage of 30 kV. The SEM chamber vacuum was better than 3×10^{-6} torr with the stage inside. The typical tensile-loading experiment lasts 1 min, and the typical tensile-loading strain rate is about 0.3 s^{-1}, according to the recorded video tape.
23. There are three soft cantilevers in series on the same side of the AFM probe. The nominal lengths *L* of these three separate silicon spring-beam type cantilevers (the cs12 contact mode AFM probe was supplied by NT-MDT) are 350, 300, and 250 μm; all have a nominal width, *w*, of 35 μm and a nominal thickness, *t*, of 1 μm. The force constant (*K*) of each can be calculated with the formula $K = Ewt3/4L3$. (Here *E* is for a silicon single crystal, 145 GPa.) We measured *L*, *w*, and *t* in an SEM and used the measured, not the nominal, values to calculate *K*.
24. T. Fujii *et al.*, *J. Vac. Sci. Technol. B* **9**, 666 (1991).
25. H. W. P. Koops *et al.*, *Jpn. J. Appl. Phys. Part 1* **33**, 7099 (1994).
26. G. G. Tibbetts and C. P. Beetz, *J. Phys. D Appl. Phys.* **20**, 292 (1987).
27. If we use the surface energy (γ) of graphite (~0.24 J m^{-2}) and the OD of this MWCNT (33 nm), the capillary force between MWCNT layers, which is equal to $2\pi OD\gamma$, is calculated to be ~50 nN; also, with use of the shear strength of graphite (~0.48 MPa) and the initial contact length between MWCNT layers (~10 mm), the shear force needed for sliding between nested layers would be ~50 nN. Because each of these values exceeds the measured upper limit force, further study of the energetics and forces involved in pullout is needed.
28. R. Bacon, *J. Appl. Phys.* **31**, 283 (1959).
29. D. E. Soule and C. W. Nezbeda, *J. Appl. Phys.* **39**, 5122 (1968).
30. M. S. Dresselhaus, G. Dresselhaus, K. Sugihara, I. L. Spain, H. A. Goldberg, *Graphite Fibers and Filaments*, Springer Series in Materials Science (Springer-Verlag, New York, 1988), vol. 5.
31. M. A. Meyers, *Dynamic Behavior of Materials* (Wiley, New York, 1994).
32. R. S. Ruoff, J. Tersoff, D. C. Lorents, S. Subramoney, B. Chan, *Nature* **364**, 514 (1993).
33. N. G. Chopra *et al.*, *Nature* **377**, 135 (1995).

34. This work was partially supported by the Office of Naval Research and the Defense Advanced Research Projects Agency under Navy grant N000014-99-1-0769, by NSF under the New Tools and Methods for Nanotechnology grant NSF-DMR 9871874, and by Zyvex. We thank R. E. Smalley's group at Rice University for the MWCNT samples and the staff at the Materials Science Center at the University of Wisconsin (UW) for their assistance (the NSF Materials Research Science and Engineering at UW provides support for the UW electron microscope facilities). We appreciate use of the Washington University TEM facility overseen by P. Gibbons; and we thank B. Files, T. Kowalewski, B. Yakobson, and R. Carpick for commenting on the manuscript. R.S.R. would like to dedicate this paper to the memory of Herbert S. Gutowsky.

7 October 1999; accepted 2 December 1999

Cloning and Heterologous Expression of the Epothilone Gene Cluster

Li Tang, Sanjay Shah, Loleta Chung, John Carney, Leonard Katz, Chaitan Khosla, Bryan Julien*

The polyketide epothilone is a potential anticancer agent that stabilizes microtubules in a similar manner to Taxol. The gene cluster responsible for epothilone biosynthesis in the myxobacterium *Sorangium cellulosum* was cloned and completely sequenced. It encodes six multifunctional proteins composed of a loading module, one nonribosomal peptide synthetase module, eight polyketide synthase modules, and a P450 epoxidase that converts desoxyepothilone into epothilone. Concomitant expression of these genes in the actinomycete *Streptomyces coelicolor* produced epothilones A and B. *Streptomyces coelicolor* is more amenable to strain improvement and grows about 10-fold as rapidly as the natural producer, so this heterologous expression system portends a plentiful supply of this important agent.

The epothilone polyketides (*1*) stabilize microtubules by means of the same mechanism of action as the anticancer agent Taxol (*2*). However, epothilones are advantageous in that they are effective against Taxol-resistant tumors and are sufficiently water soluble that they do not require deleterious solubilizing additives (*3*). For these reasons, epothilone is widely perceived as a potential successor to Taxol (*4*).

The paucity of epothilones currently obtainable represents a major impediment to clinical evaluation of this important agent. The epothilone producer *Sorangium cellulosum* yields only about 20 mg $liter^{-1}$ of the polyketides and has a 16-hour doubling time that makes produc-

KOSAN Biosciences, 3832 Bay Center Place, Hayward, CA 94545, USA.

*To whom correspondence should be addressed. E-mail: julien@kosan.com